Eur. Phys. J. C (2024) 84:44
https://doi.org/10.1140/epjc/s10052-024-12401-9

THE EUROPEAN PHYSICAL JOURNAL C

Regular Article - Theoretical Physics

Axion-like particles at future $e^- p$ collider

Karabo Mosala[1,a], **Pramod Sharma**[1,2,b], **Mukesh Kumar**[1,c], **Ashok Goyal**[3,d]

[1] School of Physics and Institute for Collider Particle Physics, University of the Witwatersrand, Wits, Johannesburg 2050, South Africa
[2] Indian Institute of Science Education and Research, Knowledge City, Sector 81, S. A. S. Nagar, PO 140306, Manauli, Punjab, India
[3] Department of Physics and Astrophysics, University of Delhi, Delhi 110 007, India

Received: 20 September 2023 / Accepted: 5 January 2024 / Published online: 17 January 2024

Abstract In this work, we explore the possibilities of producing Axion-Like Particles (ALPs) in a future $e^- p$ collider. Specifically, we focus on the proposed Large Hadron electron collider (LHeC), which can achieve a center-of-mass energy of $\sqrt{s} \approx 1.3$ TeV, enabling us to probe relatively high ALP masses with $m_a \lesssim 300$ GeV. The production of ALPs can occur through various channels, including W^+W^-, $\gamma\gamma$, ZZ, and $Z\gamma$-fusion within the collider environment. To investigate this, we conduct a comprehensive analysis that involves estimating the production cross section and constraining the limits on the associated couplings of ALPs, namely g_{WW}, $g_{\gamma\gamma}$, g_{ZZ}, and $g_{Z\gamma}$. To achieve this, we utilize a multiple-bin χ^2 analysis on sensitive differential distributions. Through the analysis of these distributions, we determine upper bounds on the associated couplings within the mass range of 5 GeV $\leq m_a \leq$ 300 GeV. The obtained upper bounds are of the order of $\mathcal{O}(10^{-1})$ for $g_{\gamma\gamma}$ (g_{WW}, g_{ZZ}, $g_{Z\gamma}$) in $m_a \in$ [5, 200 (300)] GeV considering an integrated luminosity of 1 ab^{-1}. Furthermore, we compare the results of our study with those obtained from other available experiments. We emphasize the limits obtained through our analysis and showcase the potential of the LHeC in probing the properties of ALPs.

1 Introduction

Axion-like particles (ALP) are Standard Model (SM) singlet pseudo-scalar Nambu-Goldstone bosons originally proposed to solve the strong CP problem [1–4]. Their interaction with the SM particles arises from an explicit breaking of an approximate Global Peccei-Quinn $U(1)_{PQ}$ symmetry with couplings considered as free parameters (see for example [5,6]). Subsequently, ALPs made their appearance in beyond the SM (BSM) $viz.$ composite models [7,8], Grand Unification models [9–11], extra-dimension models [12,13], super- symmetric models [14], string theories [15] etc. The axion mass and the new physics scale associated with the new physics varied over the vast range of ALP mass (sub eV to TeV) with the scale varying from electroweak to TeV and beyond. Light ALPs with masses less than eV to MeV range can modify the Cosmic Microwave Background (CMB), big Bang Nucleosynthesis (BBN), cooling and evolution of stars. Their coupling to SM particles within this mass range is severally constrained from astrophysical and cosmological observations [16–23]. Heavier ALPs in the MeV to TeV mass range though, unimportant from the astrophysical and cosmological considerations, have been the subject matter of recent studies in the context of particle physics and as dark matter portals connecting the dark-matter with the visible matter [24,25] and have been employed to explain leptonic $g-2$ anomaly with some success [26,27]. The mass and interaction of these particles with the visible matter have been explored at the high energy colliders like LEP, Tevatron, Belle-II and at the CERN Large Hadron Collider (LHC) (see for example [5,28–35]). Unlike these colliders, the future e^+e^- colliders like ILC [36], FCC-ee [37,38], CEPC [39–41], the high energy muon collider [42] and the electron-hadron collider (LHeC) using the LHC protons on the electron beam [43,44] are designed to have high luminosity, and they provide cleaner experimental environment to go beyond the LHC's precision ability and are eminently suited to determine the ALP properties. Constraints on a large range of ALP parameter space were established from LHC and the future e^+e^- collider experiments [36,45–52] through the photon fusion production to obtain the sensitivities on the ALP $\gamma\gamma$ coupling for the ALP mass in the 1 to $\sim$ 600 GeV

[a] e-mail: karabo.mosala@cern.ch
[b] e-mail: pramodsharma.iiser@gmail.com
[c] e-mail: mukesh.kumar@cern.ch (corresponding author)
[d] e-mail: agoyal45@yahoo.com

range. The possibility of detecting ALP production through electro-weak massive vector-boson fusion (VBF) processes was recently investigated in the future muon collider for m_a $\mathcal{O}$(TeV) and beyond to study the WW, ZZ, $Z\gamma$ and $\gamma\gamma$ coupling constraints [53].

In this work, we investigate the possibility of detecting ALPs production *via* VBF processes at future Large Hadron-electron Collider (LHeC) $e^- p$ colliders, focusing on producing constraints on possible couplings parameters, $g_{\gamma\gamma}$, g_{WW}, $g_{Z\gamma}$ and g_{ZZ} [54,55]. We base our study on LHeC environment, which employs the 7 TeV proton beam of the LHC and electrons from an Energy Recovery Linac (ERL) being developed for the LHeC. The choice of an ERL energy of $E_e = 60(120)$ GeV with an available proton energy $E_p = 7$ TeV would provide a centre of mass energy of $\sqrt{s} \approx 1.3(1.8)$ TeV at the LHeC [43,44,56].

This article is organised in following sections: in Sect. 2 model with effective Lagrangian and analysis framework is explained, a preliminary estimation of ALP production as a function of m_a, coupling(s) and LHeC energies are explored in Sect. 3, and results using different observable(s) are explained in Sect. 4. The comparison(s) of ours findings with existing results are discussed in Sect. 5 and a summary with discussions are followed in Sect. 6.

2 Model and framework

The interactions of ALPs with gauge bosons and SM fermions occurs via the dimension five operators, with their masses considered independently of their respective coupling strengths [29]. Hence the effective interactions between the ALPs and the electroweak gauge bosons are represented by the effective Lagrangian [30,31,57]:

$$\mathcal{L}_{\text{eff}} = \frac{1}{2}(\partial_\mu a)(\partial^\mu a) - \frac{1}{2}m_a^2 a^2 + g^2 C_{WW}\frac{a}{f_a}W^A_{\mu\nu}\tilde{W}^{\mu\nu A} + g'^2 C_{BB}\frac{a}{f_a}B_{\mu\nu}\tilde{B}^{\mu\nu}, \tag{1}$$

where $X_{\mu\nu}$ represents the field strength tensor for the $SU(2)_L$ or $U(1)_Y$, $\tilde{X}^{\mu\nu} = \frac{1}{2}\varepsilon^{\mu\nu\alpha\beta}X_{\alpha\beta}$ with $\varepsilon^{0123} = 1$ and $X \in \{B, W\}$. The ALP field and mass are represented by a and m_a, respectively. After electroweak symmetry breaking we can write the interactions between the ALP and the electroweak gauge bosons ($W^\pm, Z, \gamma$) in terms of dimension-less couplings $g_{\gamma\gamma}$, g_{WW}, $g_{Z\gamma}$ and g_{ZZ} respectively as:

$$\mathcal{L}_{\text{eff}} \supset e^2\frac{a}{f_a}g_{\gamma\gamma}F_{\mu\nu}\tilde{F}^{\mu\nu} + \frac{2e^2}{c_w s_w}\frac{a}{f_a}g_{Z\gamma}F_{\mu\nu}\tilde{Z}^{\mu\nu} + \frac{e^2}{c_w^2 s_w^2}\frac{a}{f_a}g_{ZZ}Z_{\mu\nu}\tilde{Z}^{\mu\nu} + \frac{e^2}{s_w^2}\frac{a}{f_a}g_{WW}W_{\mu\nu}\tilde{W}^{\mu\nu}. \tag{2}$$

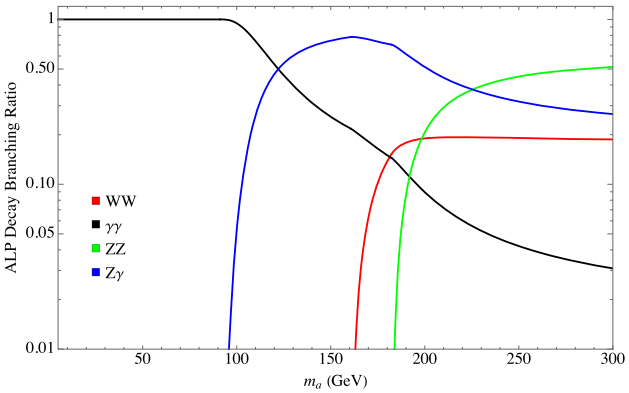

Fig. 1 The branching ratios for the decay modes of a massive ALP, $a \to W^+W^-, \gamma\gamma, ZZ$ and $Z\gamma$ as a function of its mass m_a by keeping the couplings $g_{ij} = 1$ and the scale parameter $f_a = 1$ TeV

In terms of C_{ij} ($i, j \equiv \gamma, Z, W$), the couplings g_{ij} are given by

$$\left.\begin{aligned} g_{\gamma\gamma} &= C_{WW} + C_{BB}, \\ g_{Z\gamma} &= c_w^2 C_{WW} - s_w^2 C_{BB}, \\ g_{ZZ} &= c_w^4 C_{WW} + s_w^4 C_{BB}, \\ g_{WW} &= C_{WW}. \end{aligned}\right\}, \tag{3}$$

where c_w and s_w are the cosine and sine of the Weinberg mixing angle θ_w, respectively. For all studies in this work the scale parameter is fixed to $f_a = 1$ TeV.

Using the interactions defined in Eq. (2), the relevant decay widths of ALP are given by

$$\Gamma(a \to W^+W^-) \equiv \Gamma_{WW} = \frac{e^4}{8\pi f_a^2 s_w^4}|g_{WW}|^2 m_a^3\left(1 - 4\frac{m_W^2}{m_a^2}\right)^{\frac{3}{2}}, \tag{4}$$

$$\Gamma(a \to \gamma\gamma) \equiv \Gamma_{\gamma\gamma} = \frac{e^4}{4\pi f_a^2}|g_{\gamma\gamma}|^2 m_a^3, \tag{5}$$

$$\Gamma(a \to ZZ) \equiv \Gamma_{ZZ} = \frac{e^4}{4\pi f_a^2 c_w^4 s_w^4}|g_{ZZ}|^2 m_a^3\left(1 - 4\frac{m_Z^2}{m_a^2}\right)^{\frac{3}{2}}, \tag{6}$$

$$\Gamma(a \to Z\gamma) \equiv \Gamma_{Z\gamma} = \frac{e^4}{2\pi f_a^2 c_w^2 s_w^2}|g_{Z\gamma}|^2 m_a^3\left(1 - \frac{m_Z^2}{m_a^2}\right)^{3}, \tag{7}$$

where m_W and m_Z represent the masses of the $W^\pm$ and Z bosons, respectively. As Γ_{ij} is a function of corresponding

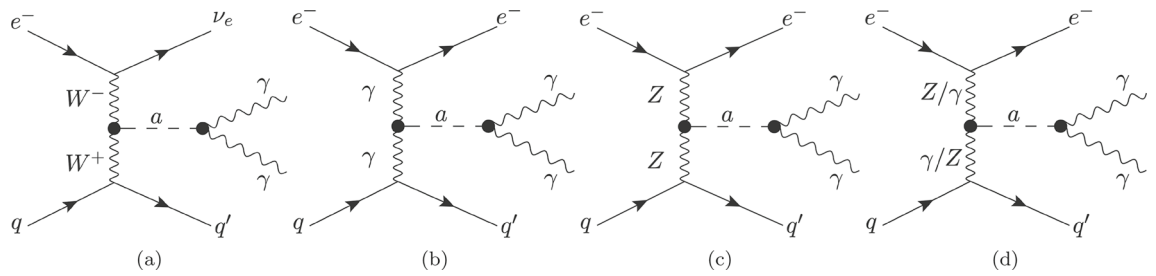

Fig. 2 Leading order representative Feynman diagrams at matrix-element level for single ALP production in (**a**) CC through $W^{\pm}$-fusion [WW] and NC through (**b**) $\gamma\gamma$, (**c**) ZZ [ZZ], and (d) $Z\gamma$-fusion [Zγ] processes in deep inelastic electron-proton collisions. A particular decay of $a \to \gamma\gamma$ is considered in this study. Here, $q, q' \equiv u, \bar{u}, d, \bar{d}, c, \bar{c}, s, \bar{s}$, or $b, \bar{b}$

coupling and masses of ALP, in this study we take variable decay width to find the limits of g_{ij} as a function of m_a. In Fig. 1, the branching ratios for the decay modes $a \to W^+W^-$, $\gamma\gamma$, ZZ, and $Z\gamma$ are plotted as a function of the mass of the ALP, m_a, assuming $g_{ij} = 1$.

Further, we define following formula to find local significance and discovery limits for a given number of signal (S) and background (B) events at a particular luminosity L, considering the total statistical and systematic uncertainties δ_s as

$$N_{\rm SD} = \frac{S}{\sqrt{S + B + (\delta_s \cdot S)^2 + (\delta_s \cdot B)^2}}, \tag{8}$$

where in terms of corresponding cross section of signal $\sigma(g_{ij})$ and background $\sigma_{\rm SM}$, $S = \sigma(g_{ij}) \cdot L$ and $B = \sigma_{\rm SM} \cdot L$, respectively.

Also to constrain the ALP−gauge coupling g_{ij}, we use a χ^2-analysis both at total cross-section and most sensitive differential-distribution level, where the χ^2 definition is given by

$$\chi^2 = \sum_{k=1}^{n} \left(\frac{N_k(g_{ij}) - N_k^{\rm SM}}{\Delta N_k} \right)^2 . \tag{9}$$

In this case, $N_k(g_{ij})$ represents number events for signal in k^{th} bin of a distribution of total n bins while $N_k^{\rm SM}$ is the corresponding background and ΔN_k is defined as:

$$\Delta N_k = \sqrt{N_k^{\rm SM}\left(1 + \delta_s^2 N_k^{\rm SM}\right)}. \tag{10}$$

For our results we consider $\delta_s = 5\%$ for a given luminosity L, and $L = 1$ ab^{-1}.

3 ALP production in $e^- p$ collider

As mentioned in Sect. 1, we are interested to probe ALP-gauge couplings by direct production of ALP through VBF processes in $e^- p$ collider. In such an environment, using the interactions defined in Sect. 2 the direct production of ALP can occur in charged-current (CC) mode through W-boson fusion as shown in Fig. 2a [WW], and in neutral-current (NC) mode through $\gamma\gamma$ (Fig. 2b), ZZ (Fig. 2c [ZZ]) and $Z\gamma$-fusion (Fig. 2d [Zγ]), where in particular we have considered the decay of ALP, $a \to \gamma\gamma$ (so we keep $g_{\gamma\gamma} = 1$ in all channels), for a given m_a. For all results, the branching ratio of ALP decay to di-photon $\mathcal{B}_{a\to\gamma\gamma}$ is taken as function of m_a, considering two cases: Case (I), where the corresponding channel's coupling is set to 1 and others to 0; and Case (II), where all couplings g_{ij} are uniformly set to 1 as depicted in Fig. 1. Here, we also note that the Zγ-channel cannot be separated from the $\gamma\gamma$-channel and hence $g_{\gamma\gamma} \neq 0$; though for Case (I) we can choose $g_{ZZ} = 0$.[1] Therefore, the notation $Z\gamma$ will refer to the effect of considering the channels shown in Fig. 2b, d (and Fig. 2c in Case (II)), and their interference.

To explore the goals of this study, we first build a model file for the interactions defined in Eq. (2) using the package FeynRules [58]. For the generation of events, we use the Monte Carlo event generator package MadGraph5_aMC@NLO[59]. Further showering, fragmentation and hadronization are done with a customized Pythia-PGS [60], and the detector level simulation performed with reasonably chosen parameters using Delphes [61] and jets were clustered using FastJet [62] with the anti-k_T algorithm [63] using the distance parameter, $R = 0.4$ as explained in Ref. [64]. The factorization and normalization scales are set to be dynamic scales for both signal and potential backgrounds. For this study, e^- polarization is assumed to be -80%. The initial requirements on transverse momentum (p_T) and rapidity (η) of jets, leptons and photons are nominal: $p_T^{j,e^-,\gamma} > 10$ GeV, $|\eta_{j,e^-,\gamma}| < 5$ and no cuts on missing energy.

With these setups the estimated cross-section of ALP production through (a) CC process: $e^- p \to \nu_e a j$, and (b) NC

[1] Important to mention: for $m_a > m_Z$, $\mathcal{B}_{a\to\gamma\gamma} < 1$ as $a \to Z\gamma$ channel opens up (Fig. 1); and deviations will become apparent in any observable for Case (I) *vs* Case (II).

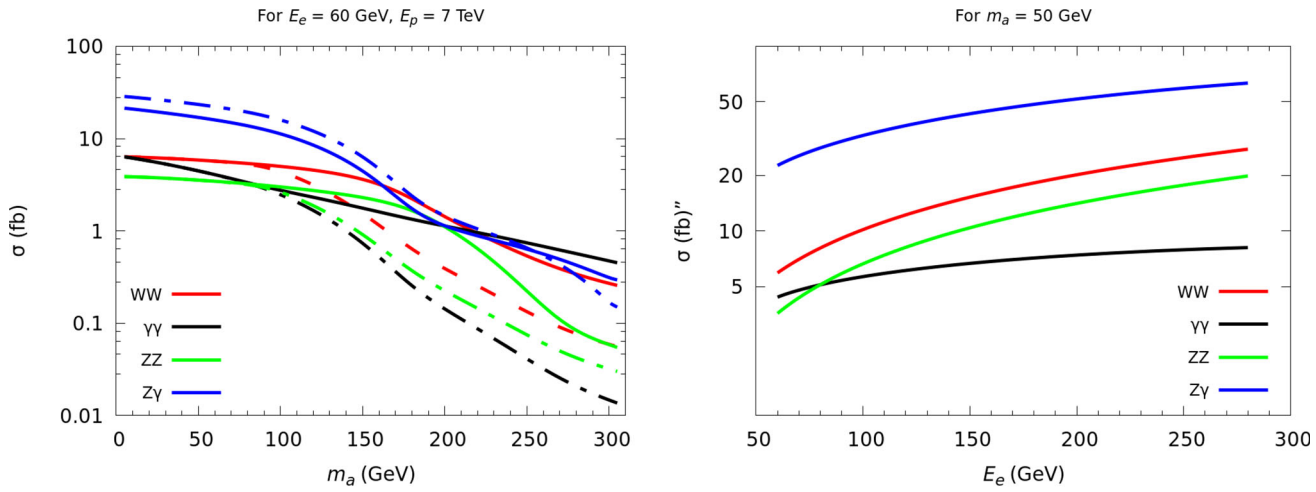

(a) (b)

Fig. 3 The production cross section of ALP production in CC and NC where $a \to \gamma\gamma$ as a function of (**a**) ALP-mass m_a, and (**b**) electron-energy E_e for fixed energy of proton $E_p = 7$ TeV. Note that the $Z\gamma$-channel can not be separated from $\gamma\gamma$-channel for Case (I) and hence here $Z\gamma$ represents total cross section considering the channels shown in Fig. 2b, d and their interference. However, in Case (II), contributions from the ZZ-channel are also included. Solid (dashed) lines represent Case (I) (Case (II))

process: $e^- p \to e^- aj$ with further decay of $a \to \gamma\gamma$ in the mass range of $5 \le m_a \le 300$ GeV is shown in Fig. 3a for a benchmark electron's energy $E_e = 60$ GeV and proton energy $E_p = 7$ TeV at LHeC. Also for a fixed $m_a = 50$ GeV, cross-section as a function of $60 \le E_e \le 300$ GeV is shown in Fig. 3b. Note that for the WW, $\gamma\gamma$ and ZZ-fusion the corresponding coupling value is taken as $g_{kk} = 1$ ($k = W, \gamma, Z$) keeping others 0, while for $Z\gamma$-fusion $g_{Z\gamma} = g_{\gamma\gamma} = 1$ keeping $g_{WW} = 0 = g_{ZZ}$ as stated in Case (I) (solid lines). For Case (II) (dashed lines), cross sections for WW, $\gamma\gamma$ and ZZ channels keep decreasing for $m_a > m_Z$, while for $Z\gamma$ its overall higher than Case (I) due to ZZ contributions. Since $m_a < m_Z$ in the case of Fig. 3b, Case (II) has no effect.

In next Sect. 4, we will focus on background generation and analysis procedures to estimate the bounds on the couplings g_{ij} using the methods described in Sect. 2. We will construct observables that are sensitive to the presence of these couplings and use them to establish the limits.

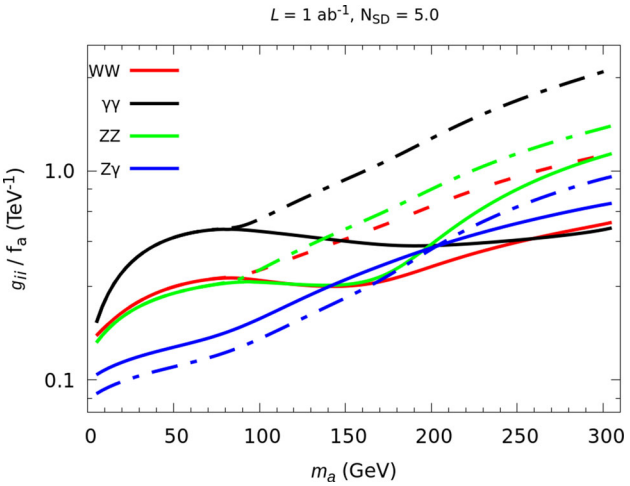

Fig. 4 The projected 5σ sensitivities for g_{ij}/f_a by using the formula in Eq. (8), on optimised events (see text for details). Solid (dashed) lines represent Case (I) (Case (II))

4 Analysis, observable and results

To generate backgrounds, we adopt similar setups as described earlier. This includes specifying the center-of-mass energy, beam polarization, and luminosity, as well as considering the relevant physics processes with "di-photon + jets" final state in CC, NC and photo-production modes and their corresponding cross sections. For $E_e = 60$ GeV and $E_p = 7$ TeV, the estimated total cross-section of background (signal) is approximately less than 6 fb (shown in Fig. 3a as a function of m_a). To optimise the signal events over the leading backgrounds additional cuts on leading and sub-leading jets, photons and leptons are applied depending on channels in this study:

- for all channels: $p_T^{j,e^-,\gamma} > 20$ GeV,
- WW: $0 < \eta_\gamma < 3$, $0 < \eta_j < 4$,
- $\gamma\gamma$: $-2 < \eta_\gamma < 3$, $-2 < \eta_j < 5$, $-2.5 < \eta_{e^-} < 2$,
- ZZ: $0 < \eta_\gamma < 3$, $0 < \eta_j < 5$, $0 < \eta_{e^-} < 5$, and
- $Z\gamma$: $0 < \eta_\gamma < 3$, $0 < \eta_j < 5$, $-2.5 < \eta_{e^-} < 1$,

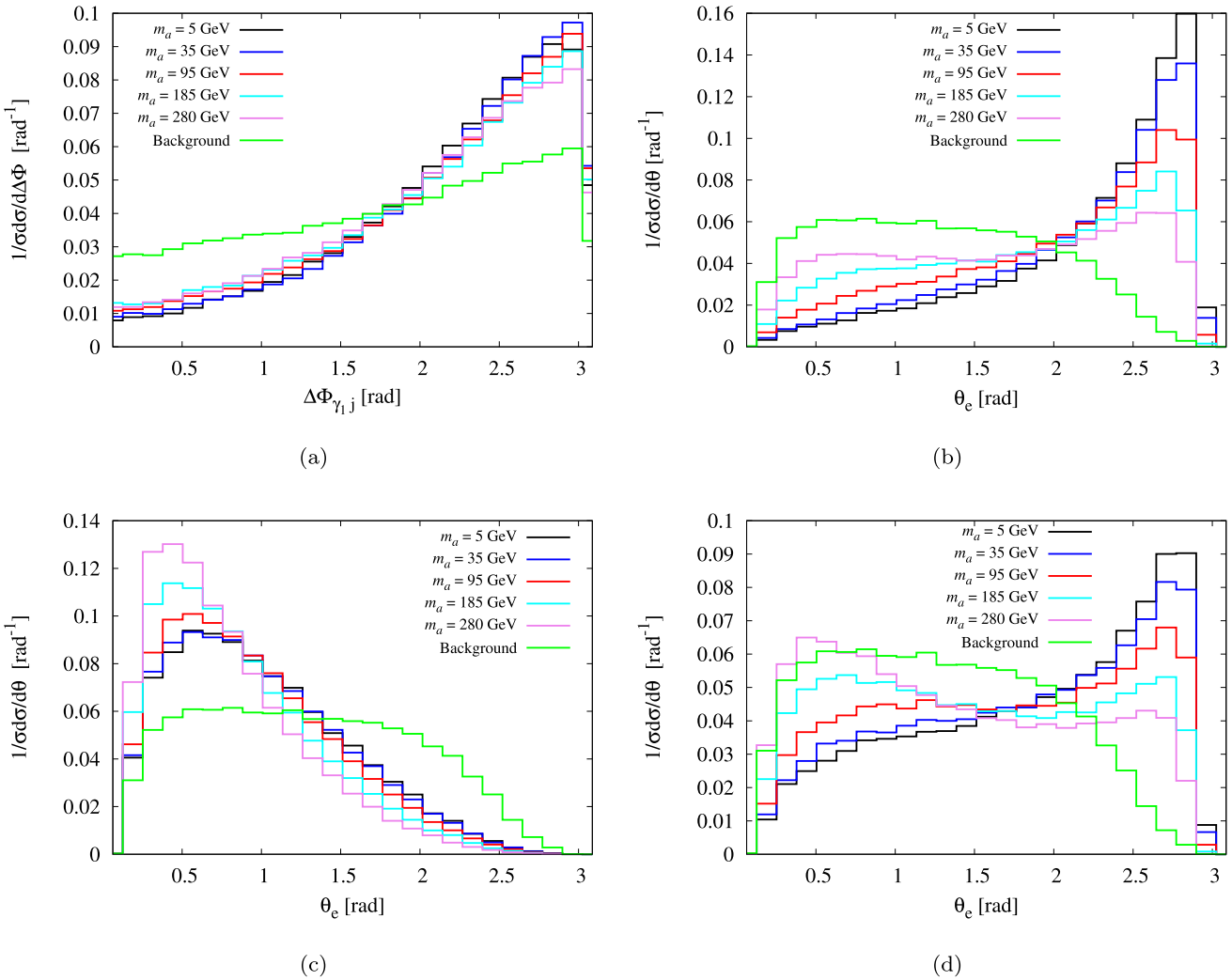

Fig. 5 Representative normalized differential distributions for Case (I) with 80% left polarized e^- beam for (**a**) WW: $\Delta\Phi_{\gamma_1 j}$ - the azimuthal angle between the two planes of the final state leading-p_T photon (γ_1) and forward jet with respect to the beam direction, and the scattered angle θ_e with respect to beam direction for the final state tagged e^- for (**b**) $\gamma\gamma$, (c) ZZ, (d) $Z\gamma$ channels, where five benchmarks m_a signal events are shown with respect to the dominant background using $E_p = 7$ TeV and $E_e = 60$ GeV with selection cuts explained in texts

in addition with invariant di-photon mass, $m_{\gamma\gamma}$, cuts as a function of corresponding signal of m_a in the window of $\sim \pm 5$ GeV. This cut significantly reduces the backgrounds in comparison to signal events. By having these optimized events we then estimate the significance and evaluate the projected sensitivities by using the formula in Eq. (8). In Fig. 4 we show the discovery limit on the coupling g_{ij}/f_a as a function of m_a by fixing $N_{\rm SD} = 5$. These limits are direct reflection of cross-section (and branching ratio) dependence on m_a as shown in Fig. 3 (Fig. 1).

Though we need to find a mechanism through which these limits must improve, and for that we studied various possible observables by considering the differential distributions and combinations of tagged final state e^-, photons, and jets for the signal as well backgrounds. In Fig. 5 we show most sensitive normalized differential distributions (for Case (I) only as representative), where for WW channel, $\Delta\Phi_{\gamma_1 j}$, the azimuthal angle between the two planes of the final state leading-p_T photon and forward jet with respect to the beam direction is shown in Fig. 5a. However, the scattered angle θ_e with respect to beam direction for the final state tagged e^- is most sensitive for $\gamma\gamma$, ZZ and $Z\gamma$ channels shown in Fig. 5b–d, respectively. It is interesting to note that the signal events in case of $\gamma\gamma$ (ZZ)-channel lies towards higher (lower) θ_e due to pure QED (V-A) structure of photon-fermion (Z-fermion) couplings, though its mixed in case of $Z\gamma$ channel. And the shape of backgrounds are due to the selection of different η-regions. So furthermore we perform a χ^2-analysis at both cross section (one-bin) and differential distribution

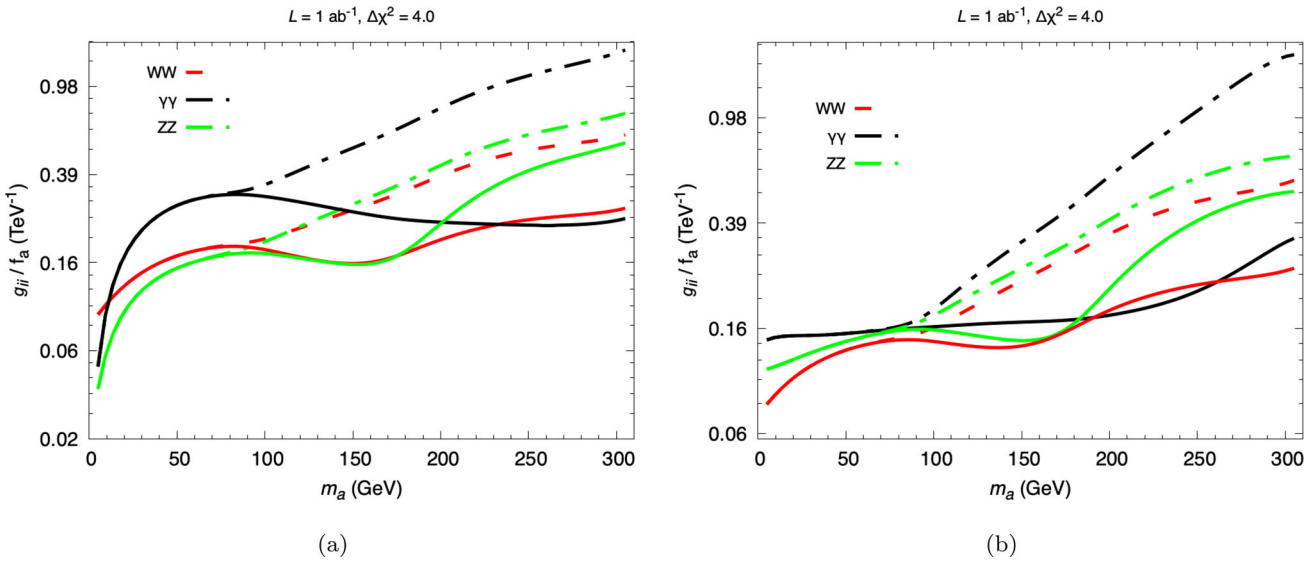

Fig. 6 The 95% C.L. contours are shown in the $g_{ii}/f_a - m_a$ plane with the observable based on χ^2-analysis for (**a**) one-bin and (**b**) multiple-bin with integrated luminosity of $L = 1$ ab^{-1}. Solid (dashed) lines represent Case (I) (Case (II))

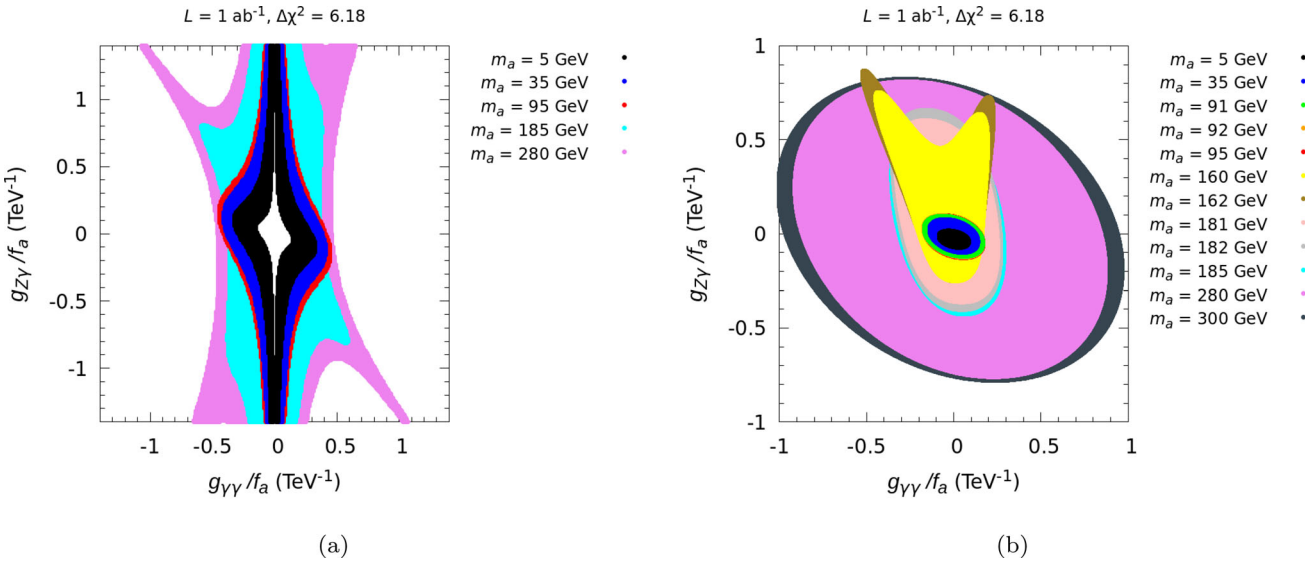

Fig. 7 The 95% C.L. contours are shown in the $g_{Z\gamma}/f_a - g_{\gamma\gamma}/f_a$ plane for selective m_a in (**a**) Case (I) and (**b**) Case (II) considering $g_{ZZ} = 0.1$; with the observable based on multiple-bins χ^2-analysis as explained in text with integrated luminosity of $L = 1$ ab^{-1}

(multiple-bin) levels[2] and apply Eq. (9) on these observable to estimate the sensitivities of g_{ij}/f_a as a function of m_a.

Note that the general structure of the $\sigma(g_{ij})$ is given as

$$\sigma(g_{ii}) = g_{ii}^2 \sigma_{ii} \times \mathcal{B}_{a\to\gamma\gamma};$$
$$\sigma(g_{Z\gamma}) = \Big(g_{\gamma\gamma}^2\sigma_{\gamma\gamma} + g_{ZZ}^2\sigma_{ZZ} + g_{Z\gamma}^2\sigma_{Z\gamma} + g_{\gamma\gamma}g_{ZZ}\sigma_{\text{inf.}}^{(1)} + g_{ZZ}g_{Z\gamma}\sigma_{\text{inf.}}^{(2)} + g_{\gamma\gamma}g_{Z\gamma}\sigma_{\text{inf.}}^{(3)}\Big) \times \mathcal{B}_{a\to\gamma\gamma}. \quad (11)$$

[2] A one-bin χ^2 analysis refers to the calculation of χ^2 for the total cross section, where the entire distribution is considered as a single bin. This approach combines all the observed and expected values across all bins and calculates the χ^2 based on the overall distribution. In a multiple-bin χ^2 analysis, the observed data are divided into different bins based on the values of the kinematic observable. The expected theoretical distribution (SM background) is also divided into the corresponding bins. The χ^2 value is then calculated for each bin by comparing the observed and expected values, taking into account the uncertainties or errors in the observed data. The individual χ^2 values for each bin are typically summed to obtain the total χ^2 value for the analysis. Therefore a multiple-bin χ^2 analysis captures the differential information present in each bin separately, providing more detailed insights into the distribution across different kinematic regions. In contrast, a one-bin χ^2 analysis provides an overall measure of the goodness-of-fit but does not account for the variations or discrepancies within individual bins.

For Case (I), $g_{ZZ} = 0$ and Eq. (11) provides the justification for the Mexican-hat shape of the χ^2 distribution, where the minimum value is $\chi^2_{\text{min.}} = 0$. In the case of a one-parameter analysis of g_{ii}/f_a *vs* m_a, we set $\chi^2 \equiv \Delta\chi^2 = 4.0$ to correspond to the 95% confidence level (C.L.). In Fig. 6a and b, we present the sensitivities of g_{ii}/f_a *vs* m_a using the one-bin and multiple-bin χ^2 analyses, respectively. From Fig. 6a, it is evident that the limits on g_{ii}/f_a perform significantly better compared to those obtained using Eq. (8) (as shown in Fig. 4). However, the multiple-bin analysis on differential distributions, as shown in Fig. 6b, outperforms the one-bin analysis (Fig. 6a) specifically for the WW and $\gamma\gamma$ channels. This indicates that considering multiple bins in the analysis provides improved sensitivity in constraining the values of g_{ii}/f_a *vs* m_a for these specific channels. The results presented in Fig. 6a and b demonstrate the enhanced performance of the multiple-bin analysis approach, emphasizing its superiority in capturing the sensitivity to g_{ii}/f_a *vs* m_a compared to the one-bin analysis, particularly for the WW and $\gamma\gamma$ channels.

Since the multiple-bin analysis performs better in these three scenario, in Fig. 7a, the limits for the $Z\gamma$ channel in the $g_{\gamma\gamma}/f_a - g_{Z\gamma}/f_a$ plane *vs* m_a are shown for five selected values of m_a for $\chi^2 \equiv \Delta\chi^2 = 6.18$ (as of two-parameter analysis for 95% C.L.) using this approach only. It is observed that the shape of the limits is asymmetric with respect to $g_{\gamma\gamma} = g_{Z\gamma} \approx 0$, where the limits also blow up. This asymmetry can be attributed to the presence of negative and positive interference effects. According to Eq. (11), the region around $g_{\gamma\gamma} = g_{Z\gamma} \approx 0$ can be understood. In this region, all values of $g_{Z\gamma}$ can satisfy the χ^2 criterion below the 2σ standard deviation when $g_{\gamma\gamma}$ tends to zero. However, we have excluded the region near $g_{\gamma\gamma} = 0$ in order to fulfill the minimum requirement of an ALP signal for the study. The observed spikes in the contour is due to the negative contribution from interference, which leads to infinite values for both couplings. The presence of four spikes can be attributed to the even powers of the couplings in the cross-section Eq. (11). When the value of $g_{\gamma\gamma}$ is non-zero, these spikes disappear, and the contour takes on a circular shape due to the negligible contribution from interference.

In Fig. 7b, limits on the $g_{\gamma\gamma}/f_a - g_{Z\gamma}/f_a$ plane *vs* m_a are presented for Case (II). To achieve a 95% C.L. corresponding to $\Delta\chi^2 = 6.18$, we establish a benchmark point by setting $g_{ZZ} = 0.1$. This choice is made because, for $g_{ZZ} = 1$, corresponding values of $\Delta\chi^2$ exceed 6.18. Significant deviations at the mass points for m_a corresponding to the $Z\gamma$, W^+W^-, and ZZ resonances are readily apparent.

5 Comparison of $g_{ij}(m_a)$ to existing bounds

In Fig. 8, a comparison of coupling limits is presented in the $|g_{ij}|/f_a - m_a$ plane at the 95% confidence level (C.L.), along with constraints from various experiments and theory predictions. It is important to note that a given measurement can depend on multiple ALP couplings. Representing the corresponding bound in the 2D ($|g_{ij}|/f_a$, m_a) plane requires making theoretical assumptions, which can vary significantly from constraint to constraint. These differences should be considered for a proper comparison. In Fig. 8, the bounds derived in the present work (shown as the brown line) represent the 95% C.L. limits. They are derived assuming full decay of the ALP to di-photons. In order to compare the limits on $Z\gamma$-channel, given in Fig. 7a (Fig. 7b) as a correlation between $g_{Z\gamma}$ and $g_{\gamma\gamma}$ (and g_{ZZ}) due to the interference, we show a standalone comparison of constraints on $g_{Z\gamma}$ with previous studies keeping $g_{\gamma\gamma} = 0.1$ (and $g_{ZZ} = 0.1$) for Case (I) (Case (II)).

The limits on $g_{\gamma\gamma}$ and $g_{Z\gamma}$ at higher ALP masses are obtained from collider studies, where the ALP decays resonantly either to hadrons or to photon pairs. The relevant process are from $e^+e^- \to \gamma$ + hadrons, studied by the L3 experiment [65] and the leading bounds from photon pair production at the Large Hadron Collider (LHC) in proton-proton collisions [45,66] (labeled as "LHC" for measurements from ATLAS and CMS), as well as from light-by-light scattering $\gamma\gamma \to \gamma\gamma$ measured in lead-lead (Pb-Pb) collisions [67,68] (labeled as "Light-by-light (LHC)"). The measurement of the total Z decay width at LEP provides constraints up to $m_a \lesssim m_Z$ [29,69].

For ALP masses above 100 GeV, the dominant bounds come from resonant triboson searches [69]. Additionally, nonresonant searches in diboson production via gluon fusion at the LHC (labeled as "Nonresonant ggF") provide constraints on all four ALP interactions. Each nonresonant bound is extracted from a specific process $gg \to a^* \to V_1V_2$ ($V = \gamma, Z, W^\pm$). The constraint on $g_{\gamma\gamma}$ is derived in Ref. [51], those on g_{WW} and $g_{\gamma Z}$ in Ref. [70], and the constraint on g_{ZZ} in Ref. [71].

The bound obtained from the Z width measurement at LEP does not require additional assumptions. The bounds from nonresonant ggF, which include nonresonant $gg \to a^* \to V_1V_2$ processes, scale with the inverse of the axion-gluon coupling (g_{gg}) and are completely lifted when the ALP coupling to gluons $C_{GG} \to 0$. In the figure, they are normalized to $g_{gg} = 1$ (for details see Ref. [72]).

Bounds labeled as "γ + had" and LHC (various) assume gluon dominance, i.e., $g_{gg} \gg g_{V_1V_2}$, and in this limit, they are largely independent of C_{GG} (see Ref. [5]). Among these, bounds on $g_{\gamma\gamma}$ labeled as "LHC" additionally assume negligible branching fractions to fermions and heavy electroweak bosons in the mass region where they are kinematically allowed. The limit from light-by-light scattering, shown in red, assumes $\mathcal{B}_{a\to\gamma\gamma} = 1$, which corresponds to vanishing couplings to gluons and light fermions. The triboson con-

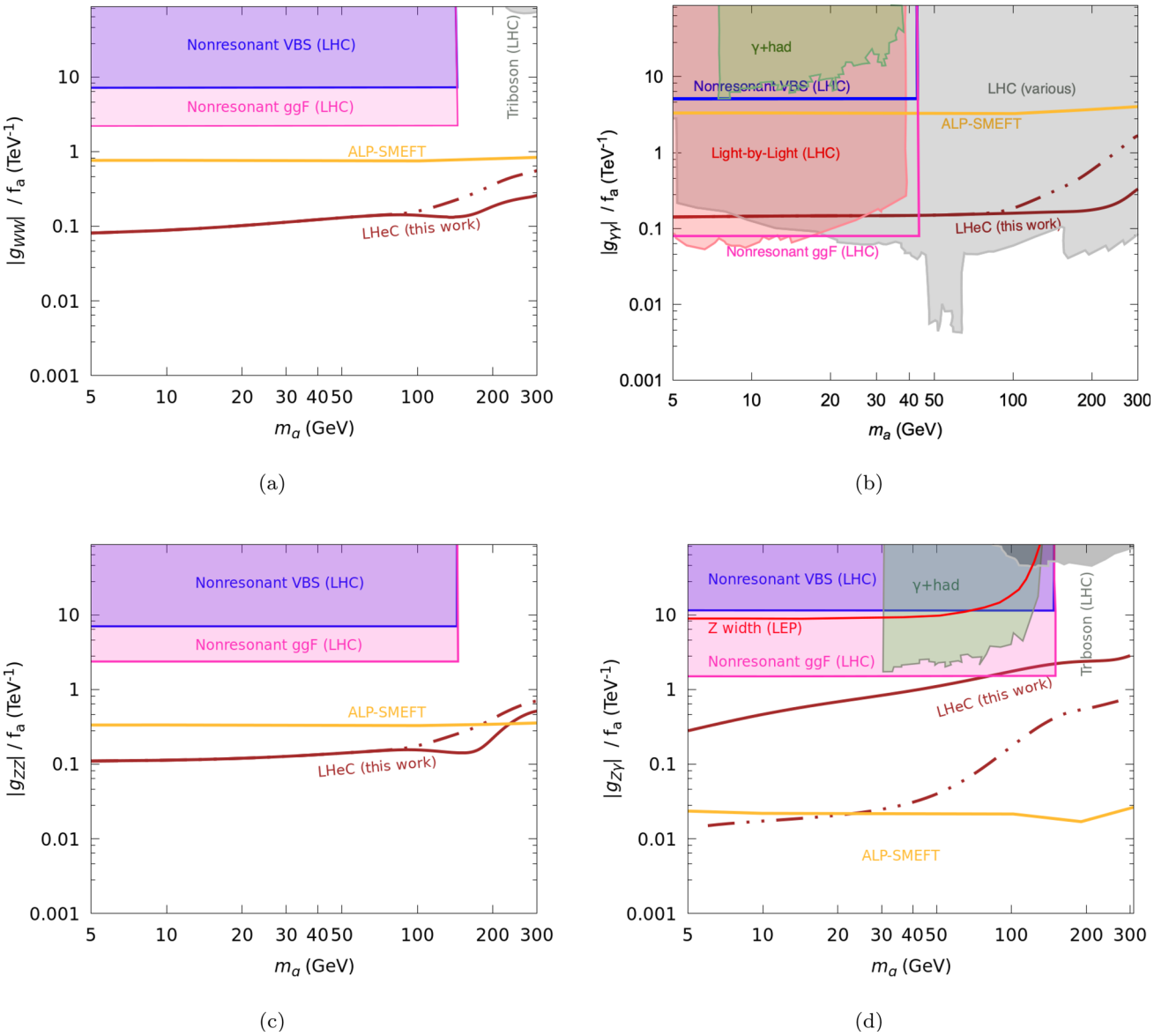

Fig. 8 The 95% C.L. contours in the $|g_{ij}|/f_a - m_a$ plane are shown for the limits obtained from multiple-bin χ^2-analysis with an integrated luminosity of $L = 1$ ab^{-1}. Corresponding available limits from LHC, γ+hadron, Z width at LEP, and ALP-SMEFT are also shown for comparison (see text for details). Our constraints given in Fig. 7a (Fig. 7b) for $g_{Z\gamma}$ are correlated with $g_{\gamma\gamma}$ (and g_{ZZ}) due to the interference. For standalone comparison of constraints on $g_{Z\gamma}$ with previous studies, we keep $g_{\gamma\gamma} = 0.1$ (and $g_{ZZ} = 0.1$); where brown solid (dashed) line represents Case (I) (Case (II))

straints on g_{WW} and $g_{Z\gamma}$ make use of the photophobic ALP scenario [69].

A recent study has utilized ALP-SMEFT interference to establish limits on various ALP couplings [35]. These bounds exhibit particular effectiveness in the ALP mass range where constraints from flavor and astrophysics searches tend to weaken. We have applied these bounds to our specific cases using Eq. (3) and compared the resulting limits in Fig. 8.

Limits on the effective ALP-photon coupling have been derived from exotic Higgs and Z decay searches at the LHC in [30,31], and the probed parameter space is found to be in agreement with the results presented in this work.

Overall the limits found in this work performs better sensitivity for all three ALP couplings, namely, g_{WW}, g_{ZZ} and $g_{Z\gamma}$ comparing to available studies in different collider scenario, whereby, the limits on $g_{\gamma\gamma}$ are competitive with respect to few cases. In ALP-SMEFT bounds, the performance of $g_{Z\gamma}$ is relatively poor.

6 Summary and discussions

In this article, we investigated the potential for the production of relatively high-mass Axion-Like Particles (ALPs) in an electron-proton ($e^- p$) environment. Specifically, we focused on the proposed energy of the Large Hadron-electron Collider (LHeC) with a center-of-mass energy of $\sqrt{s} \approx 1.3$ TeV and an integrated luminosity of $L = 1$ ab^{-1}. Although exploring high masses beyond 300 GeV is less likely due to the limited cross section achievable with the available energy and luminosity, we examined the limits on coupling measurements as prediction for such masses based on our analysis procedure. These limits serve as approximate predictions that can be investigated further if the electron energy (E_e) is increased to higher values.

In Fig. 8 we provide a comprehensive overview of the coupling limits in the $|g_{ij}|/f_a - m_a$ plane, taking into account various experimental and theoretical constraints, and highlights the strengths and limitations of each measurement in constraining ALP couplings. To analyze and capture the differential information in the distribution of kinematic observables, a multiple-bin χ^2 analysis is preferable in contrast to one-bin, where we observed the limits performance are better. Also the limits on g_{WW}, g_{ZZ} and $g_{Z\gamma}$ comparing to available studies in different collider scenario are better at LHeC for considered range of m_a, whereby, the limits on $g_{\gamma\gamma}$ are competitive with respect to few scenario.

By studying the possibilities of ALP production in the $e^- p$ environment at the LHeC, we contribute to the understanding of ALP physics and provide insights into the potential for probing relatively higher masses and coupling strengths in future experiments. While numerous studies on probing ALPs have been conducted, this article stands among the first to explore the potential of a proposed future $e^- p$ collider, specifically at the suggested energy levels of the LHeC.

Acknowledgements PS would like to acknowledge the School of Physics at the University of the Witwatersrand, where the majority of this work was conducted during his visit. Their support and resources were invaluable in carrying out this research. AG thanks SERB, G.O.I. Under CRG/2018/004889.

Data Availability Statement This manuscript has no associated dat or the data will not be deposited. [Authors' comment: For this work authors used publicly available data where necessary, and are referenced properly.].

Funded by SCOAP[3].

References

1. R.D. Peccei, H.R. Quinn, Phys. Rev. Lett. **38**, 1440–1443 (1977)
2. R.D. Peccei, H.R. Quinn, Phys. Rev. D **16**, 1791–1797 (1977)
3. S. Weinberg, Phys. Rev. Lett. **40**, 223–226 (1978)
4. F. Wilczek, Phys. Rev. Lett. **40**, 279–282 (1978)
5. G. Alonso-Álvarez, M.B. Gavela, P. Quilez, Eur. Phys. J. C **79**(3), 223 (2019). arXiv:1811.05466 [hep-ph]
6. J. Bonilla, I. Brivio, M.B. Gavela, V. Sanz, JHEP **11**, 168 (2021). arXiv:2107.11392 [hep-ph]
7. J.E. Kim, Phys. Rev. D **31**, 1733 (1985)
8. G. Leder, Nucl. Phys. B **497**, 334–344 (1997). arXiv:hep-ph/9610552
9. M. Feindt, CERN-PPE-91-90
10. H.M. Georgi, L.J. Hall, M.B. Wise, Nucl. Phys. B **192**, 409–416 (1981)
11. V.A. Rubakov, JETP Lett. **65**, 621–624 (1997). arXiv:hep-ph/9703409
12. K.R. Dienes, E. Dudas, T. Gherghetta, Phys. Rev. D **62**, 105023 (2000). arXiv:hep-ph/9912455
13. T. Legero, T. Wilk, A. Kuhn, G. Rempe, Appl. Phys. B **8**, 77 (2003)
14. B. Lillard, T.M.P. Tait, JHEP **11**, 005 (2017). arXiv:1707.04261 [hep-ph]
15. P. Svrcek, E. Witten, JHEP **06**, 051 (2006). arXiv:hep-th/0605206
16. Hirao Kaigo, Moroi Takeo, Phys. Rev. D **3**, 104 (2021)
17. Nguyen David V, Sarnaaik Dimple, Boddy Kimberly K, Nadler Ethan O, Gluscevic Vera, Phys. Rev. D **10**, 104 (2021)
18. D. Green, S. Rajendran, JHEP **10**, 013 (2017). arXiv:1701.08750 [hep-ph]
19. D. Baumann, D. Green, B. Wallisch, Phys. Rev. Lett. **117**(17), 171301 (2016). arXiv:1604.08614 [astro-ph.CO]
20. G. Krnjaic, S.D. McDermott, Phys. Rev. D **101**(12), 123022 (2020). arXiv:1908.00007 [hep-ph]
21. G.G. Raffelt, Lect. Notes Phys. **741**, 51–71 (2008). arXiv:hep-ph/0611350
22. J.S. Lee, arXiv:1808.10136 [hep-ph]
23. J.H. Chang, R. Essig, S.D. McDermott, JHEP **09**, 051 (2018). arXiv:1803.00993 [hep-ph]
24. L. Darmé, F. Giacchino, E. Nardi, M. Raggi, JHEP **06**, 009 (2021). arXiv:2012.07894 [hep-ph]
25. P. Agrawal, M. Bauer, J. Beacham, A. Berlin, A. Boyarsky, S. Cebrian, X. Cid-Vidal, D. d'Enterria, A. De Roeck, M. Drewes et al., Eur. Phys. J. C **81**(11), 1015 (2021). arXiv:2102.12143 [hep-ph]
26. B. Long, Phys. Rev. D **94**(1), 011503 (2016). arXiv:1508.06084 [hep-ph]
27. M. Ablikim et al., BESIII. Phys. Rev. Lett. **124**(24), 241803 (2020). arXiv:2004.13910 [hep-ex]
28. D. d'Enterria, arXiv:2102.08971 [hep-ex]
29. I. Brivio, M.B. Gavela, L. Merlo, K. Mimasu, J.M. No, R. del Rey, V. Sanz, Eur. Phys. J. C **77**(8), 572 (2017). arXiv:1701.05379 [hep-ph]
30. M. Bauer, M. Neubert, A. Thamm, JHEP **12**, 044 (2017). arXiv:1708.00443 [hep-ph]
31. M. Bauer, M. Heiles, M. Neubert, A. Thamm, Eur. Phys. J. C **79**(1), 74 (2019). arXiv:1808.10323 [hep-ph]
32. M. Chala, G. Guedes, M. Ramos, J. Santiago, Eur. Phys. J. C **81**(2), 181 (2021). arXiv:2012.09017 [hep-ph]

33. M. Bauer, M. Neubert, S. Renner, M. Schnubel, A. Thamm, JHEP **04**, 063 (2021). arXiv:2012.12272 [hep-ph]
34. M. Bauer, M. Neubert, S. Renner, M. Schnubel, A. Thamm, JHEP **09**, 056 (2022). arXiv:2110.10698 [hep-ph]
35. A. Biekötter, J. Fuentes-Martín, A.M. Galda, M. Neubert, JHEP **09**, 120 (2023). arXiv:2307.10372 [hep-ph]
36. H.Y. Zhang, C.X. Yue, Y.C. Guo, S. Yang, Phys. Rev. D **104**(9), 096008 (2021). arXiv:2103.05218 [hep-ph]
37. M. Bicer et al., TLEP Design Study Working Group. JHEP **01**, 164 (2014). arXiv:1308.6176 [hep-ex]
38. A. Abada, M. Abbrescia, S.S. AbdusSalam et al., Eur. Phys. J. Spec. Top. **228**, (2014)
39. I. Bozovic-Jelisavcic, R. Manqi, Z. Hongbo, Z. Kai, H. Suen, PoS **ICHEP2018**, 429 (2019)
40. J.B. Guimarães da Costa et al., [CEPC Study Group]. arXiv:1811.10545 [hep-ex]
41. F. An, Y. Bai, C. Chen, X. Chen, Z. Chen, J. Guimaraes da Costa, Z. Cui, Y. Fang, C. Fu, J. Gao et al., Chin. Phys. C **43**(4), 043002 (2019). arXiv:1810.09037 [hep-ex]
42. D. Stratakis et al., [Muon Collider], arXiv:2203.08033 [physics.acc-ph]
43. J.L. Abelleira Fernandez et al., [LHeC Study Group], J. Phys. G **39**, 075001 (2012). arXiv:1206.2913 [physics.acc-ph]
44. J.L. Abelleira Fernandez et al., [LHeC Study Group]. arXiv:1211.5102 [hep-ex]
45. J. Jaeckel, M. Jankowiak, M. Spannowsky, Phys. Dark Univ. **2**, 111–117 (2013). arXiv:1212.3620 [hep-ph]
46. C. Baldenegro, S. Fichet, G. von Gersdorff, C. Royon, JHEP **06**, 131 (2018). arXiv:1803.10835 [hep-ph]
47. A. Flórez, A. Gurrola, W. Johns, P. Sheldon, E. Sheridan, K. Sinha, B. Soubasis, Phys. Rev. D **103**(9), 095001 (2021). arXiv:2101.11119 [hep-ph]
48. W.J. Marciano, A. Masiero, P. Paradisi, M. Passera, Phys. Rev. D **94**(11), 115033 (2016). arXiv:1607.01022 [hep-ph]
49. S.C. İnan, A.V. Kisselev, Chin. Phys. C **45**(4), 043109 (2021). arXiv:2007.01693 [hep-ph]
50. D. Buttazzo, D. Redigolo, F. Sala, A. Tesi, JHEP **11**, 144 (2018). arXiv:1807.04743 [hep-ph]
51. M.B. Gavela, J.M. No, V. Sanz, J.F. de Trocóniz, Phys. Rev. Lett. **124**(5), 051802 (2020). arXiv:1905.12953 [hep-ph]
52. S.C. İnan, A.V. Kisselev, JHEP **06**, 183 (2020). arXiv:2003.01978 [hep-ph]
53. T. Han, T. Li, X. Wang, arXiv:2203.05484 [hep-ph]
54. C.X. Yue, H. Wang, X.J. Cheng, Y.Q. Wang, Phys. Rev. D **107**(11), 115025 (2023). arXiv:2305.19561 [hep-ph]
55. C.X. Yue, M.Z. Liu, Y.C. Guo, Phys. Rev. D **100**(1), 015020 (2019). arXiv:1904.10657 [hep-ph]
56. O. Bruening, M. Klein, Mod. Phys. Lett. A **28**(16), 1330011 (2013). arXiv:1305.2090 [physics.acc-ph]
57. H. Georgi, D.B. Kaplan, L. Randall, Phys. Lett. B **169**, 73–78 (1986)
58. A. Alloul, N.D. Christensen, C. Degrande, C. Duhr, B. Fuks, Comput. Phys. Commun. **185**, 2250 (2014)
59. J. Alwall, M. Herquet, F. Maltoni, O. Mattelaer, T. Stelzer, JHEP **1106**, 128 (2011)
60. T. Sjostrand, S. Mrenna, P.Z. Skands, JHEP **05**, 026 (2006). arXiv:hep-ph/0603175
61. J. de Favereau et al., DELPHES 3. JHEP **02**, 057 (2014). arXiv:1307.6346 [hep-ex]
62. M. Cacciari, G.P. Salam, G. Soyez, Eur. Phys. J. C **72**, 1896 (2012). arXiv:1111.6097 [hep-ph]
63. M. Cacciari, G.P. Salam, G. Soyez, JHEP **04**, 063 (2008). arXiv:0802.1189 [hep-ph]
64. M. Kumar, X. Ruan, R. Islam, A.S. Cornell, M. Klein, U. Klein, B. Mellado, Phys. Lett. B **764**, 247–253 (2017). arXiv:1509.04016 [hep-ph]
65. O. Adriani et al., [L3], Phys. Lett. B **292**, 472–484 (1992)
66. A. Mariotti, D. Redigolo, F. Sala, K. Tobioka, Phys. Lett. B **783**, 13–18 (2018). arXiv:1710.01743 [hep-ph]
67. A.M. Sirunyan et al., [CMS], Phys. Lett. B **797**, 134826 (2019). arXiv:1810.04602 [hep-ex]
68. G. Aad et al., [ATLAS], JHEP **03**, 243 (2021) (**erratum: JHEP 11 (2021), 050**). arXiv:2008.05355 [hep-ex]
69. N. Craig, A. Hook, S. Kasko, JHEP **09**, 028 (2018). arXiv:1805.06538 [hep-ph]
70. S. Carra, V. Goumarre, R. Gupta, S. Heim, B. Heinemann, J. Kuechler, F. Meloni, P. Quilez, Y.C. Yap, Phys. Rev. D **104**(9), 092005 (2021). arXiv:2106.10085 [hep-ex]
71. A. Tumasyan et al., [CMS], JHEP **04**, 087 (2022). arXiv:2111.13669 [hep-ex]
72. J. Bonilla, I. Brivio, J. Machado-Rodríguez, J.F. de Trocóniz, JHEP **06**, 113 (2022). arXiv:2202.03450 [hep-ph]